

Overcoming the black body limit in plasmonic and graphene near-field thermophotovoltaic systems

Ognjen Ilic,^{1,*} Marinko Jablan,² John D. Joannopoulos,¹ Ivan Celanovic,³ and Marin Soljačić¹

¹*Department of Physics, Massachusetts Institute of Technology, 77 Massachusetts Avenue, Cambridge, Massachusetts, 02139, USA*

²*Department of Physics, University of Zagreb, Bijenička c. 32, 10000 Zagreb, Croatia*

³*Institute for Soldier Nanotechnologies, Massachusetts Institute of Technology, 77 Massachusetts Avenue, Cambridge, Massachusetts 02139, USA*

[*ilico@mit.edu](mailto:ilico@mit.edu)

Abstract: Near-field thermophotovoltaic (TPV) systems with carefully tailored emitter-PV properties show large promise for a new temperature range (600 – 1200K) solid state energy conversion, where conventional thermoelectric (TE) devices cannot operate due to high temperatures and far-field TPV schemes suffer from low efficiency and power density. We present a detailed theoretical study of several different implementations of thermal emitters using plasmonic materials and graphene. We find that optimal improvements over the black body limit are achieved for low bandgap semiconductors and properly matched plasmonic frequencies. For a pure plasmonic emitter, theoretically predicted generated power density of $14 \frac{W}{cm^2}$ and efficiency of 36% can be achieved at 600K (hot-side), for 0.17eV bandgap (InSb). Developing insightful approximations, we argue that large plasmonic losses can, contrary to intuition, be helpful in enhancing the overall near-field transfer. We discuss and quantify the properties of an optimal near-field photovoltaic (PV) diode. In addition, we study plasmons in graphene and show that doping can be used to tune the plasmonic dispersion relation to match the PV cell bandgap. In case of graphene, theoretically predicted generated power density of $6(120) \frac{W}{cm^2}$ and efficiency of 35(40)% can be achieved at 600(1200)K, for 0.17eV bandgap. With the ability to operate in intermediate temperature range, as well as high efficiency and power density, near-field TPV systems have the potential to complement conventional TE and TPV solid state heat-to-electricity conversion devices.

© 2012 Optical Society of America

OCIS codes: (040.5350) Photovoltaic; (310.6628) Subwavelength structures, nanostructures; (240.6680) Surface plasmons.

References and links

1. S. Rytov, Y.A. Kratsov, and V. I. Tatarskii, *Principles of Statistical Radiophysics* (Springer-Verlag, 1987).
2. D. Polder and M. Van Hove, "Theory of radiative heat transfer between closely spaced bodies," *Phys. Rev. B* **4**, 3303–3314 (1971).
3. J. B. Pendry, "Radiative exchange of heat between nanostructures," *J. Phys.: Condens. Matter* **11**, 6621–6633 (1999).

4. C. H. Park, H. A. Haus, and M. S. Weinberg, "Proximity-enhanced thermal radiation," *J. Phys. D: Appl. Phys.* **35**, 2857–2863 (2002).
5. C. Hargreaves, "Anomalous radiative transfer between closely-spaced bodies," *Phys. Lett. A* **30**, 491–492 (1969).
6. A. Narayanaswamy, S. Shen, and G. Chen, "Near-field radiative heat transfer between a sphere and a substrate," *Phys. Rev. B* **78**, 115303 (2008).
7. S. Shen, A. Narayanaswamy, and G. Chen, "Surface phonon polaritons mediated energy transfer between nanoscale gaps," *Nano Lett.* **9**, 2909–2913 (2009).
8. E. Rousseau, A. Siria, G. Jourdan, F. Comin, J. Chevrier, and J.-J. Greffet, "Radiative heat transfer at the nanoscale," *Nat. Photonics* **3**, 514–517 (2009).
9. R. DiMatteo, P. Greiff, D. Seltzer, D. Meulenbergh, E. Brown, E. Carlen, K. Kaiser, S. Finberg, H. Nguyen, J. Azarkevich, P. Baldasaro, J. Beausang, L. Danielson, M. Dashiell, D. DePoy, H. Ehsani, W. Topper, and K. Rahner, "Micron-gap thermophotovoltaics (MTPV)," *Proc. 6th Conf. Thermophotovoltaic Generation of Electricity* (2004).
10. M. Whale and E. Cravalho, "Modeling and performance of microscale thermophotovoltaic energy conversion devices," *IEEE Trans. Energy Convers.* **17**, 130–142 (2002).
11. M. Laroche, R. Carminati, and J.-J. Greffet, "Near-field thermophotovoltaic energy conversion," *J. Appl. Phys.* **100**, 063704 (2006).
12. S. Basu, Y.-B. Chen, and Z. M. Zhang, "Microscale radiation in thermophotovoltaic devices – a review," *Int. J. Energy Res.* **31**, 689–716 (2007).
13. M. Francoeur, R. Vaillon, and M. P. Mengüç, "Thermal impacts on the performance of nanoscale-gap thermophotovoltaic power generators," *IEEE Trans. Energy Convers.* **26**, 686–698 (2011).
14. K. Park, S. Basu, W. King, and Z. Zhang, "Performance analysis of near-field thermophotovoltaic devices considering absorption distribution," *J. Quant. Spectrosc. Radiat. Transfer* **109**, 305–316 (2008).
15. S. Basu, Z. M. Zhang, and C. J. Fu, "Review of near-field thermal radiation and its application to energy conversion," *Int. J. Energy Res.* **33**, 1203–1232 (2009).
16. J. Pan, H. Choy, and C. G. Fonstad, Jr., "Very large radiative transfer over small distances from a black body for thermophotovoltaic applications," *IEEE Trans. Electron Devices* **47**, 241–249 (2000).
17. A. Narayanaswamy and G. Chen, "Surface modes for near field thermophotovoltaics," *Appl. Phys. Lett.* **82**, 3544–3546 (2003).
18. K. Joulain, J.-P. Mulet, F. Marquier, R. Carminati, and J.-J. Greffet, "Surface electromagnetic waves thermally excited: Radiative heat transfer, coherence properties and casimir forces revisited in the near field," *Surf. Sci. Rep.* **57**, 59–112 (2005).
19. J. R. Dixon and J. M. Ellis, "Optical properties of *n*-type indium arsenide in the fundamental absorption edge region," *Phys. Rev.* **123**, 1560–1566 (1961).
20. G. W. Gobeli and H. Y. Fan, "Infrared absorption and valence band in indium antimonide," *Phys. Rev.* **119**, 613–620 (1960).
21. S. A. Maier, *Plasmonics - Fundamentals and Applications* (Springer (US), 2010).
22. J. D. Joannopoulos, S. G. Johnson, J. N. Winn, and R. D. Meade, *Photonic Crystals: Molding the Flow of Light*, 2nd ed. (Princeton University Press, 2008).
23. J. L. Pan, "Radiative transfer over small distances from a heated metal," *Opt. Lett.* **25**, 369–371 (2000).
24. J.-P. Mulet, K. Joulain, R. Carminati, and J.-J. Greffet, "Enhanced radiative heat transfer at nanometric distances," *Microscale Thermophys. Eng.* **6**, 209–222 (2002).
25. J. J. Loomis and H. J. Maris, "Theory of heat transfer by evanescent electromagnetic waves," *Phys. Rev. B* **50**, 18517–18524 (1994).
26. I. Celanovic, F. O'Sullivan, M. Ilak, J. Kassakian, and D. Perreault, "Design and optimization of one-dimensional photonic crystals for thermophotovoltaic applications," *Opt. Lett.* **29**, 863–865 (2004).
27. R. Venkatasubramanian, E. Siivola, T. Colpitts, and B. O'Quinn, "Thin-film thermoelectric devices with high room-temperature figures of merit," *Nature* **413**, 597–602 (2001).
28. M. Zenker, A. Heinzl, G. Stollwerck, J. Ferber, and J. Luther, "Efficiency and power density potential of combustion-driven thermophotovoltaic systems using GaSb photovoltaic cells," *IEEE Trans. Electron Devices* **48**, 367–376 (2001).
29. E. Rephaeli and S. Fan, "Absorber and emitter for solar thermo-photovoltaic systems to achieve efficiency exceeding the Shockley-Queisser limit," *Opt. Express* **17**, 15145–15159 (2009).
30. P. Bermel, M. Ghebrebrhan, W. Chan, Y. X. Yeng, M. Araghchini, R. Hamam, C. H. Marton, K. F. Jensen, M. Soljačić, J. D. Joannopoulos, S. G. Johnson, and I. Celanovic, "Design and global optimization of high-efficiency thermophotovoltaic systems," *Opt. Express* **18**, A314–A334 (2010).
31. J. B. Pendry, L. Martn-Moreno, and F. J. Garcia-Vidal, "Mimicking surface plasmons with structured surfaces," *Science* **305**, 847–848 (2004).
32. W. L. Barnes, A. Dereux., and T. W. Ebessen, "Surface plasmon subwavelength optics," *Nature* **424**, 824–830.
33. S. H. Mousavi, A. B. Khanikaev, B. Neuner, Y. Avitzour, D. Korobkin, G. Ferro, and G. Shvets, "Highly confined hybrid spoof surface plasmons in ultrathin metal-dielectric heterostructures," *Phys. Rev. Lett.* **105**, 176803 (2010).

34. A. D. Rakic, A. B. Djurišić, J. M. Elazar, and M. L. Majewski, "Optical properties of metallic films for vertical-cavity optoelectronic devices," *Appl. Opt.* **37**, 5271–5283 (1998).
35. W. Steinmann, "Experimental verification of radiation of plasma oscillations in thin silver films," *Phys. Rev. Lett.* **5**, 470–472 (1960).
36. L. D. Landau and E. M. Lifshitz, *Statistical Physics, Part 2* (Pergamon Press, 1980).
37. I. Hamberg and C. G. Granqvist, "Evaporated Sn-doped In_2O_3 films: Basic optical properties and applications to energy-efficient windows," *J. Appl. Phys.* **60**, R123–R160 (1986).
38. S. H. Brewer and S. Franzen, "Calculation of the electronic and optical properties of indium tin oxide by density functional theory," *Chem. Phys.* **300**, 285–293 (2004).
39. P. West, S. Ishii, G. Naik, N. Emani, V. Shalaev, and A. Boltasseva, "Searching for better plasmonic materials," *Laser Photonics Rev.* **4**, 795–808 (2010).
40. K. S. Novoselov, A. K. Geim, S. V. Morozov, D. Jiang, Y. Zhang, S. V. Dubonos, I. V. Grigorieva, and A. A. Firsov, "Electric field effect in atomically thin carbon films," *Science* **306**, 666–669 (2004).
41. M. Jablan, H. Buljan, and M. Soljačić, "Plasmonics in graphene at infrared frequencies," *Phys. Rev. B* **80**, 245435 (2009).
42. B. Wunsch, T. Stauber, F. Sols, and F. Guinea, "Dynamical polarization of graphene at finite doping," *New J. Phys.* **8**, 318 (2006).
43. E. H. Hwang and S. Das Sarma, "Dielectric function, screening, and plasmons in two-dimensional graphene," *Phys. Rev. B* **75**, 205418 (2007).
44. A. I. Volokitin and B. N. J. Persson, "Near-field radiative heat transfer between closely spaced graphene and amorphous SiO_2 ," *Phys. Rev. B* **83**, 241407 (2011).
45. B. N. J. Persson and H. Ueba, "Heat transfer between graphene and amorphous SiO_2 ," *J. Phys. Condens. Matter* **22**, 462201 (2010).
46. L. A. Falkovsky, "Optical properties of graphene," *J. Phys. Conf. Ser.* **129**, 012004 (2008).
47. R. G. Yang, A. Narayanaswamy, and G. Chen, "Surface-plasmon coupled nonequilibrium thermoelectric refrigerators and power generators," *J. Comput. Theor. Nanosci.* **2**, 75–87 (2005).
48. J. E. Sipe, "New green-function formalism for surface optics," *J. Opt. Soc. Am. B* **4**, 481–489 (1987).
49. K. Joulain, J. Drevillon, and P. Ben-Abdallah, "Noncontact heat transfer between two metamaterials," *Phys. Rev. B* **81**, 165119 (2010).
50. H. A. Haus, "Thermal noise in dissipative media," *J. Appl. Phys.* **32**, 493–500 (1961).

1. Introduction

An inherent limitation of a thermophotovoltaic (TPV) system is the upper limit on spectral emissivity of the emitter - the black body limit. This is true for TPV systems operating in the *far field*, where the separation between the emitter and the photovoltaic cell is large enough to limit the energy transfer only to modes propagating in air. Contrary to this is the *near-field* mode of operation, whereby reducing the gap between two surfaces allows for tunnelling of evanescent modes. It has been theoretically argued [1–4] and experimentally shown [5–8] that sub-micron separations can greatly enhance the energy transfer compared to that in the far field and even that of the black body.

In this manuscript, we analyze a TPV system consisting of a plasmonic emitter and a short-wavelength infrared bandgap photovoltaic (PV) cell. Plasmonic materials support surface plasmon polaritons (SPP), electromagnetic excitations propagating along the surface of the material, that can be thermally excited. In the near field, the density of these surface modes strongly increases at frequencies close to the surface plasmon frequency $\omega_p/\sqrt{2}$, where ω_p is the material plasma frequency. In photovoltaic cells, photons with energies less than the bandgap energy cannot create electron-hole pairs, whereas for high-energy photons the difference in photon energy and the bandgap energy is lost due to thermalization. The almost monochromatic nature of SPPs thus allows for efficient energy transfer, when surface plasmon frequency is tuned close to the bandgap energy.

This paper is divided into five sections. In section 2, we develop physical intuition and investigate the optimal parameters of the analyzed near-field TPV system. In section 3, we analyze silver and indium tin oxide (ITO), materials that support surface plasmons, as potentially useful thermal emitters. In section 4, we study plasmons in graphene and energy transfer in a graphene-PV system. Finally, we summarize the results in section 5.

2. Optimal near-field TPV design: Model and Theory

Radiation transfer at subwavelength scales and applications to thermophotovoltaic devices has been a subject of much research [9–17]. In many of these references, the main interest was in emitter and/or the photovoltaic (PV) cell parameters that maximize radiation transfer, energy conversion efficiency, power output, etc. Here, we provide an intuitive explanation for the role that each of the parameters plays in overall energy transfer in the near field.

A near-field TPV system, as illustrated in Fig. 1, consists of a higher temperature plasmonic emitter and a colder photovoltaic cell, separated by a distance D . We model both components as non-magnetic, semi-infinite slabs, with frequency-dependent permittivity responses $\varepsilon_i(\omega)$ where $i = 1, 0, 2$ corresponds to emitter, air gap, and PV cell, respectively. Throughout the manuscript, it is assumed that the PV cell is operating at room temperature $T_2 \approx 300\text{K}$. Both the emitter and the PV cell are connected to a thermal reservoir, maintaining non-equilibrium temperature difference. We begin by recalling the equations that govern the non-contact radi-

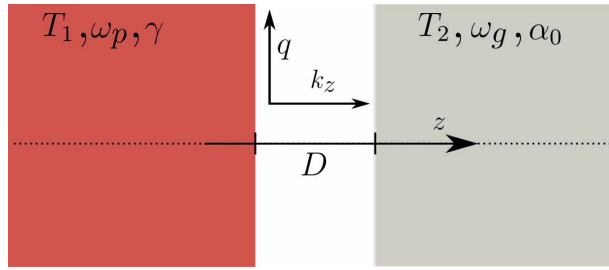


Fig. 1. Schematic illustration of a near-field TPV system. Plasmonic emitter, characterized by the plasma frequency ω_p and damping γ , operates at temperature T_1 . Next to it, a distance D away, is the photovoltaic cell at temperature T_2 , characterized by the bandgap energy ω_g , photon absorption coefficient α_0 , and the refractive index n . The parallel and the perpendicular wave vectors are q and k_z , respectively.

ation transfer in the near and the far field. For two semi-infinite slabs, separated by air gap of size D , the contribution of evanescent and propagating modes to the net radiation transfer, as calculated using fluctuational electrodynamics, is given by [18]

$$H_{\text{evan}}^{s,p} = \frac{1}{\pi^2} \int_0^\infty d\omega [\Theta(\omega, T_1) - \Theta(\omega, T_2)] \int_{\omega/c}^\infty dq q \frac{\text{Im}(r_{01}^{s,p}) \text{Im}(r_{02}^{s,p})}{|1 - r_{01}^{s,p} r_{02}^{s,p} e^{2ik_z D}|^2} e^{-2|k_z|D} \quad (1)$$

$$H_{\text{prop}}^{s,p} = \frac{1}{\pi^2} \int_0^\infty d\omega [\Theta(\omega, T_1) - \Theta(\omega, T_2)] \int_0^{\omega/c} dq q \frac{(1 - |r_{01}^{s,p}|^2)(1 - |r_{02}^{s,p}|^2)}{4|1 - r_{01}^{s,p} r_{02}^{s,p} e^{2ik_z D}|^2} \quad (2)$$

Here r_{ij}^l corresponds l -polarization reflectivity coefficient at the i - j interface, $\Theta(\omega, T) = \hbar\omega / [\exp(\hbar\omega/k_b T) - 1]$ is the mean energy of a photon at temperature T , known as the Boltzmann factor, and k_{z0} is the perpendicular wave vector k_z in the gap medium. The far field energy transfer between a black body ($r_{0i} = 0$) at T_1 and a black body at T_2 calculated using Eq. (2) would be $H_{\text{prop}} = \sigma (T_1^4 - T_2^4)$, where σ is the Stefan-Boltzmann constant.

The permittivity of a pure plasmonic emitter is given by the standard Drude-Lorentz expression $\varepsilon_1(\omega) = 1 - \omega_p^2 / (\omega^2 + i\omega\gamma)$, where ω_p is the plasma frequency and γ is the plasma damping term. Furthermore, we restrict our analysis of near-field transfer, H_{evan} , to only p -polarized modes, as these modes dominate the evanescent ($q \gg \omega/c$) transfer regime in non-magnetic materials [3].

Design requirements for an optimal photovoltaic cell operating in the far field are different from an optimal photovoltaic cell operating in the near field. A far field photovoltaic cell needs

to minimize reflections to reach high efficiencies. This is achieved using an anti-reflection coating, such as several stacked dielectric layers designed to cancel reflected waves of desired wavelengths. Characteristics which make for a good near-field photovoltaic cell will be discussed later; presently, we treat the photovoltaic cell as a semiconductor, with dielectric permittivity approximately modeled as

$$\epsilon_2(\omega) = \left(n + i \frac{\alpha}{2k_0} \right)^2 \quad \text{where} \quad \alpha(\omega) = \begin{cases} 0 & , \omega < \omega_g \\ \alpha_0 \sqrt{\frac{\omega - \omega_g}{\omega_g}} & , \omega > \omega_g \end{cases} \quad (3)$$

where n is the refractive index, $k_0 = 2\pi/\lambda$ where λ is the photon wavelength in vacuum, and ω_g is the bandgap frequency. Square root dependence of the absorption coefficient is a characteristic of direct bandgap semiconductors. For example, indium arsenide, InAs, is a direct bandgap semiconductor where $\omega_g = 0.36\text{eV}$; in the above model $\alpha_0 \approx 1.3 \times 10^4 \text{cm}^{-1}$ matches experimentally measured values (at room temperature) [19] reasonably well for frequencies near the bandgap, as discussed in section 2.3. Similarly, indium antimonide, InSb, is also a direct bandgap semiconductor ($\omega_g = 0.17\text{eV}$) where $\alpha_0 \approx 0.7 \times 10^4 \text{cm}^{-1}$ is a reasonable fit for the experimentally measured absorption values (at room temperature) [20]. The simple model in Eq. (3) is not meant to completely characterize optical properties of a given semiconductor but, instead, to capture general trends and quantify the near-field heat transfer to a reasonable degree of accuracy. We would like to point out two things regarding this model: first, accurate modeling of the PV cell is complicated by discrepancies in experimentally reported values of semiconductor absorption in the literature; and second, at higher frequencies our fit becomes worse (section 2.3). However, modes at such high frequencies do not contribute much to the power transfer, due to the exponentially decaying Boltzmann factor $\Theta(\omega, T)$. For most of the calculated values of power density (Tables 1 and 2), the difference between using the model given by Eq. (3) and the reported values in literature [19,20] is under 5% (maximum difference of under 15%). Calculated efficiencies are even less sensitive to this distinction, with differences mostly unnoticeable to two significant figures.

2.1. Plasmon damping γ

For many SPP applications plasmon damping is undesirable and low values for γ are favored [21]. For energy transfer in the near field, however, the opposite can be true. A rough, qualitative, picture of the role of γ can be obtained as follows: in the extreme near field ($q \gg \omega/c$), and for very weak damping, surface plasmon local density of states is proportional to the imaginary part of permittivity [18], which is in turn proportional to γ ; consequently, very small γ implies low power transfer. On the other hand, a large value of γ completely dampens the surface mode and the radiation transfer diminishes. While the situation in a TPV system is more complicated, this argument correctly implies that there is an optimal value of γ for which transfer of energy is maximized. To get a better understanding, we show (Appendix A) how a complicated expression in Eq. (1) for radiation transfer in the near field can be approximated as a lorentzian lineshape in frequency. We first define $(\epsilon_2 - 1)/(\epsilon_2 + 1) \equiv \chi' + i\chi''$, where ϵ_2 is given by Eq. (3), and χ', χ'' are real. In general, both χ' and χ'' depend on frequency and obtaining a closed-form expression for the dispersion relation is non-trivial. However, for realistic PV parameters ($n = 3.51$, $\alpha_0 \approx 10^4 \text{cm}^{-1}$), χ' is approximately constant and $\chi''/\chi' \ll 1$, as discussed in section 2.3. Rewriting Eq. (1) as

$$H_{\text{evan}}^p = \frac{1}{\pi^2} \int_0^\infty d\omega [\Theta(\omega, T_1) - \Theta(\omega, T_2)] \int_{\omega/c}^\infty dq q \Pi(\omega, q) \quad (4)$$

we can express the *spectral transfer function* for a given channel q as

$$\Pi(\omega, q) = \frac{\gamma\beta(\omega, q)}{4[\omega - \omega_0(q)]^2 + [\gamma + \beta(\omega, q)]^2} \quad \text{where} \quad \beta(\omega, q) \equiv \frac{\omega_p^2 - 2\omega_0(q)^2}{2\omega_0(q)} \frac{\chi''(\omega)}{\chi'(\omega)} \quad (5)$$

where ω_0 and the dispersion relation is given by Eq. (17). Equation (5) is the central equation of this section. It separates plasmon damping coefficient γ from other parameters, and PV cell parameters only enter through dimensionless χ''/χ' ratio, which we label the PV cell *admissivity* in the near field. Figure 2 shows the comparison between the spectral transfer function calculated using Eq. (5) and using Eq. (1), for several values of parallel wave vector q . In each case, we see that Eq. (5) is indeed a very good approximation. Limits of its validity are discussed in Appendix A. In accordance with the dispersion relation Eq. (17) of the two-interface system

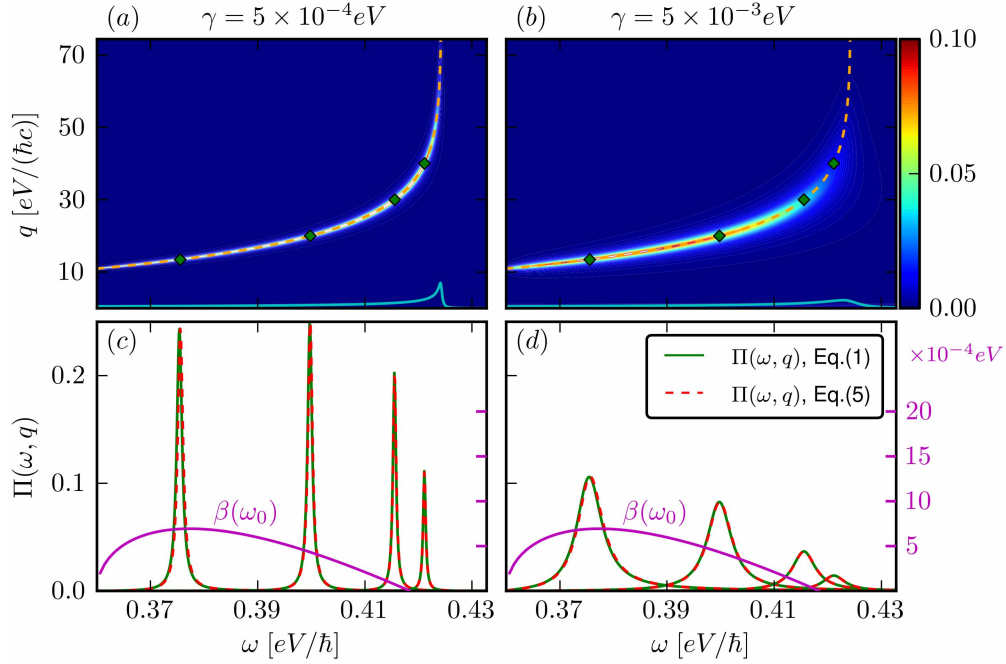


Fig. 2. Contour plot of $\Pi(\omega, q)$ from Eq. (1) for (a) $\gamma = 5 \times 10^{-4} eV$, (b) $\gamma = 5 \times 10^{-3} eV$. Dashed line shows the dispersion relation from Eq. (17), and the solid cyan line shows the dispersion relation of a surface plasmon in air. In (c) and (d), solid (dashed) line corresponds to the spectral transfer function $\Pi(\omega, q)$ calculated using Eq. (1) (Eq. (5)), for four different values of q . On a separate scale, β is plotted as a function of ω_0 (magenta), where the x -axis for ω_0 and ω is shared. Plasma frequency, PV gap frequency and PV absorption coefficient are $\omega_p = 0.6 eV$, $\omega_g = 0.36 eV$ and $\alpha_0 = 1.3 \times 10^4 cm^{-1}$, respectively. Separation is $D = 10 nm$ ($1/D \approx 20 eV/\hbar c$).

shown in Fig. 1, bringing the PV cell in extreme vicinity of the emitter shifts the power transfer to much higher q -vectors compared to the dispersion of the surface plasmon in air. This is a direct result of the delocalized nature of isolated surface plasmons, making the joint dispersion relation particularly sensitive to separation between two interfaces.

The integrated radiation transfer increases with γ , for small γ ; to show this, we note that in

the limit $\gamma \ll \beta$ the width of Π is $\approx \beta$, i.e:

$$\Pi(\omega, q) = \frac{\gamma\beta(\omega, q)}{4[\omega - \omega_0(q)]^2 + [\gamma + \beta(\omega, q)]^2} \approx \gamma \frac{\beta(\omega, q)}{4[\omega - \omega_0(q)]^2 + \beta(\omega, q)^2} \quad (6)$$

To analyze the large γ limit, the Boltzmann factor $\Theta(\omega, T)$ must be included. For photon energies on the order of an electron-volt and reasonably high emitter temperatures, $\Theta(\omega, T_2)$ can be ignored (for $\omega = 0.2eV$, $T_1 = 600K$, we have $\Theta(\omega, T_2)/\Theta(\omega, T_1) \approx 0.02$). We define

$$A(q) = \int_{\omega_g}^{\infty} d\omega \Theta(\omega, T_1) \Pi(\omega, q) \quad (7)$$

where $A(q)$ is the *spectral cross-section* for a given wave vector, q . Integration limit is chosen such that only photons with energies greater than the bandgap are included. When γ is very large, $\gamma \gg \beta$, $\omega - \omega_0$, the dominant dependence in Eq. (5) is $1/\gamma$ for low enough frequencies for which $\Theta(\omega, T_1)$ is effectively non-zero. As a result, the heat transfer goes down with increasing γ . To get a sense of the optimal value of plasmon damping, we note that for $\omega_0 = 0.38eV$ (corresponding to maximum value of β , Fig. 2(c)), $\omega_g = 0.36eV$, and $T_1 = 600K$, the spectral cross-section $A(q)$ is maximized for $\gamma = 6.8 \times 10^{-3}eV$, and decays thereafter.

It is interesting to note that Eq. (5) has the same functional form as the transmission coefficient of a waveguide-cavity-waveguide system, obtained using temporal coupled mode theory equations [22]. There, the transmission through a cavity is maximized when the coefficients that measure cavity coupling to each waveguide, $1/\tau_1$ and $1/\tau_2$, are equal. This is the condition for *critical coupling*. In this case, the critical coupling is achieved when $\gamma = \beta$; an example of this is shown in Fig. 2(c) (second from the left peak, where $\gamma = \beta = 5 \times 10^{-4}eV$). However, critical coupling has low transmission over a broad range of frequencies (low spectral cross-section), and is not suitable for enhancing broadband radiation transfer. Note that when both media are plasmonic (i.e. $\epsilon_2 = \epsilon_1$, analyzed in Appendix A), the system is always critically coupled due to symmetry.

Finally, the dispersion relation, Eq. (17), of this system tells us that the modes that dominate the near-field energy transfer are highly-evanescent. In Fig. 2, we see that, at $D = 10nm$, these modes have characteristic wave vectors almost two orders of magnitude larger than the normalized vacuum frequency. Whether or not such extremely evanescent modes participate in energy transfer has been a topic of much debate [4, 16, 23–25]. This debate is centered around the prediction that integrated energy transfer would diverge as $1/D^2$, as two slabs are brought closer together. While this is deemed unphysical and a violation of energy conservation by some authors [16, 23], others have defended the result, noting it is based on a macroscopic formalism that does not in itself impose the limit on the separation, but would break down when separations approach atomic distances [4, 24, 25]. We note from Fig. 2 that characteristic distances for maximum wave-vector values of relevant modes ($\approx 40eV/\hbar c$) are on the order of $\approx 5nm$, well above the atomic separation limit.

2.2. Plasma and gap frequency, ω_p , ω_g

Many variables in this system make for a rich parameter space. In general, it is hard to isolate the contribution of a specific parameter and quantify the behavior of the integrated radiation transfer based solely on that parameter. In that respect, looking at how radiation transfer depends on ω_p and ω_g is relevant because the main takeaway points remain valid for a wide range of γ , T_1 and D .

We look at the ratio of the near-field transfer between a plasmonic emitter and the PV cell, versus the far-field transfer between two black bodies. Radiation transfer between two black bodies in the far field is known to be the upper-limit on radiation transfer between any two

media of given temperatures in the far field. The first expression, H_{evan} , is obtained from Eq. (1), whereas the second, H_{bb} , is obtained from Eq. (2), with $r_{01} = r_{02} = 0$. Both expressions are integrated over all wave vectors q ; however, in contrast to equations Eq. (1) and Eq. (2), the integral over frequency is limited to frequencies higher than ω_g .

Figure 3 shows this ratio for different ω_p, ω_g . Two key points from this figure remain true for a range of γ, T_1, D , and could be stated as follows: there is an optimal frequency separation $\Delta \equiv \omega_p/\sqrt{2} - \omega_g$, and transfer ratio increases with decreasing ω_g, ω_p . To understand the first point, we note that for small Δ (red line in Fig. 3), there is little absorption ($\beta \approx 0$), and the

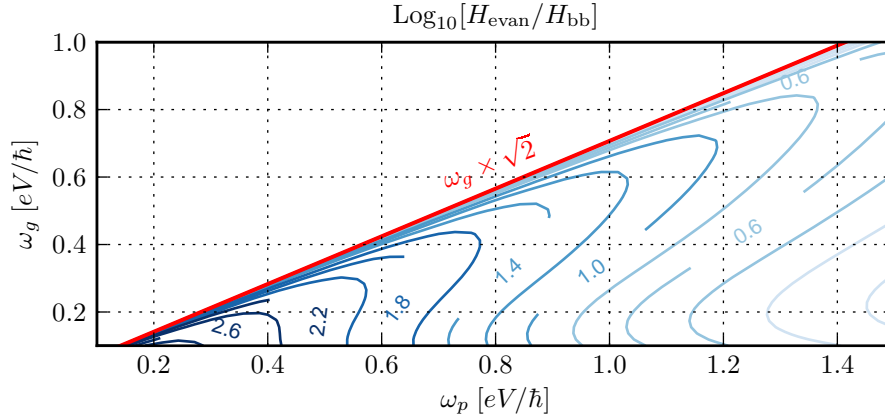


Fig. 3. Contour plot of logarithm of transfer ratio versus ω_p, ω_g , for the plasmonic emitter-PV system in Fig. 1. Plasmon damping is $\gamma = 5 \times 10^{-3} \text{eV}$, and temperature is $T_1 = 600\text{K}$, with other parameters being the same as in Fig. 2.

ratio rapidly grows for increasing Δ . For a large Δ , however, the surface plasmon frequency is too far from ω_g and the transfer between two black bodies grows faster in the $[\omega_g, \omega_p/\sqrt{2}]$ range. In other words, there is a mismatch between the optimal plasmonic density of states occurring at frequencies closer to $\omega_p/\sqrt{2}$ and PV cell absorption, characterized by β . With the optimal Δ fixed, simultaneously lowering ω_g and ω_p shifts the dispersion relation Eq. (17) and concentrates (due to behavior of β as a function of ω_g) radiation transfer to lower frequencies where the average energy per mode is exponentially higher. This is particularly beneficial for surface plasmon modes in the near field, where the density of photonic modes is much higher (no limit on q) than for a black body (at the same frequency) in the far field. One also notices that, due to the scale invariant nature of Maxwell's equations, lowering frequency is equivalent to decreasing the separation, resulting in the increase of (near-field) transfer.

2.3. PV cell in the near field

We already mentioned how requirements for an efficient photovoltaic cell in the far field are different from a photovoltaic cell operating in the near field. So far, we have focused on a bare semiconductor as the PV cell, with the dielectric response given by Eq. (3). Previously, we showed how increasing plasmon damping leads to enhanced radiation transfer. However, given the symmetry of Eq. (5) with respect to γ and β , similar reasoning can be applied to β as well. We calculated that, for a given mode where $\beta = 5 \times 10^{-4} \text{eV}$, there was an optimal value of γ that maximizes the spectral cross-section. However, the symmetry of β and γ implies that, ideally, we would like both parameters to be larger. For a larger β , the optimal γ would naturally be larger as well, and the overall transfer would grow. From this perspective, making a more efficient near-field PV cell would mean that the PV cell admittance, χ''/χ' , should be made as

high as possible (note, however, that this analysis is valid only when $\chi''/\chi' \ll 1$).

On the other hand, the optimal relationship between the plasma frequency ω_p and the gap frequency ω_g , as discussed in the previous section, implies that both frequencies should be as low as possible, with $\omega_p/\sqrt{2}$ in the vicinity of ω_g . These two facts imply that an efficient near-field PV cell should have a large absorption coefficient (and hence large admittivity) right near the bandgap frequency, and decay afterwards. Theoretically, one way of achieving this is by having a step-like absorption curve $\alpha(\omega)$. Instead of Eq. (3), we write

$$\varepsilon_2(\omega) = \left(n + i \frac{\alpha}{2k_0} \right)^2 \quad \text{where} \quad \alpha(\omega) = \begin{cases} 0 & , \omega < \omega_g \\ \alpha_0 & , \omega > \omega_g \end{cases} \quad (8)$$

In Fig. 4, we compare values for χ' and χ'' for when α is given by Eq. (3), calculated experimentally, and when it is given by Eq. (8). First, for the purpose of a near-field PV cell, modeling

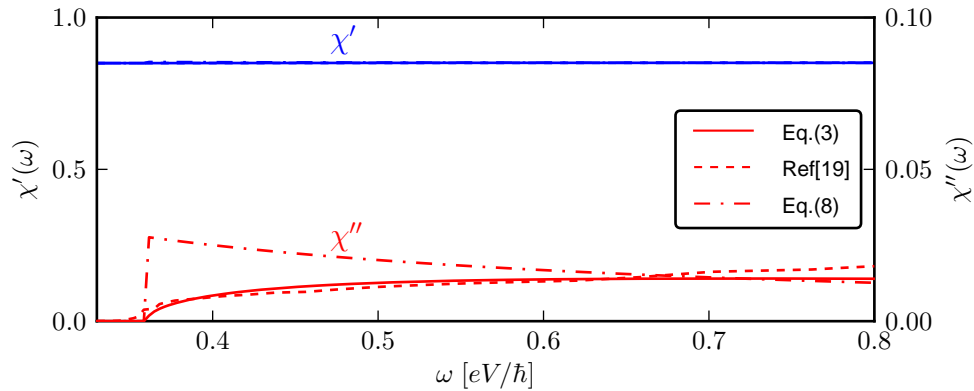


Fig. 4. Plot of χ' (blue) and χ'' (red) for a semiconductor as a function of frequency, with $\omega_g = 0.36 eV$ and $n = 3.51$. Three lines correspond to the absorption coefficient α calculated using square-root dependence, Eq. (3), with $\alpha_0 = 1.3 \times 10^4 cm^{-1}$, experimental values for InAs from Ref. [19], and using step-like dependence, Eq. (8), with same α_0 . We see that both PV cell approximations, $\chi' \approx 0.85$, and $\chi''/\chi' \ll 1$, are satisfied in this frequency range.

absorption of InAs as a square-root dependence on energy was an appropriate approximation. Second, a step-like dependence given by Eq. (8) focuses the radiation transfer to frequencies right around ω_g : for parameter values as in Fig. 2, and the same value of $\alpha_0 = 1.3 \times 10^4 cm^{-1}$, the overall power transfer H_{evan} is up to a factor of $3 \times$ stronger for step-like absorption dependence than for the square-root one. This implies that step-like dependence, while being the simplest model for PV cell absorption, also overestimates the near-field transfer.

2.4. Temperature dependence, efficiency and power density

In this section, we explore how the ratio of the power transferred in the near field, H_{evan} , to the power transferred between two black bodies in the far field, H_{bb} , depends on the emitter temperature. For an appropriate choice of parameters, this dependence can be increasing, decreasing, or non-monotonic. This flexibility can allow a possible design of a near-field device that would operate at temperatures that are usually too low for a conventional thermophotovoltaic device but too high for a conventional thermoelectric one.

In Fig. 5, we plot this ratio for several different values of plasma frequencies and damping, for emitter temperature range of $600K - 1500K$. As we previously calculated, for $\omega_p = 0.6 eV$, the

optimal damping coefficient was $\gamma = 6.8 \times 10^{-3} eV$, when β was maximized. Figure 5 confirms

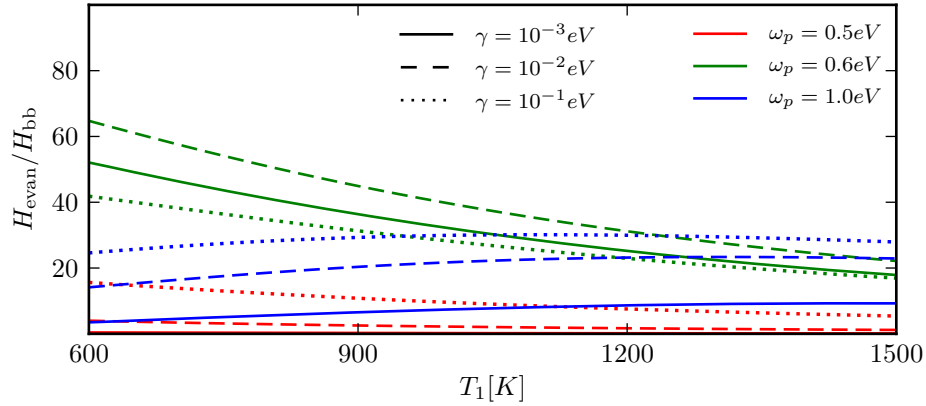


Fig. 5. Radiation transfer ratio, as a function of emitter temperature T_1 for a pure plasmonic emitter-PV cell near-field TPV system. The ratio is plotted for several values of ω_p and γ , with other parameters being the same as in Fig. 2, namely $\omega_g = 0.36 eV$, $D = 10 nm$.

that this result is a decent estimate of optimal γ . The other two cases can also be understood using Eq. (5) and Eq. (7). When surface plasmon frequency is below the gap frequency (i.e. $\omega_p = 0.5 eV$), only the tails of the lorentzian above ω_g contribute to the near field transfer. Since the width of the lorentzian in Eq. (5) is dependent on γ , stronger damping is preferable, as shown in Fig. 5. Finally, for large ω_p , examining spectral cross-section $H(q)$ similarly as before, we find the optimal γ , corresponding to when β is maximum, is $\approx 0.05 eV$. Again, Fig. 5 shows this is a reasonable estimate for the damping coefficient.

For a fixed value of damping (i.e. $\gamma = 10^{-1} eV$), changing the plasma frequency significantly alters the temperature dependence in the plotted temperature range. As an example, this dependence can be non-monotonic, as shown for the $\omega_p = 1.0 eV$ case in Fig. 5. For well-matched gap and plasma frequencies, the case of $\omega_p = 0.6 eV$ in Fig. 5, the dependence can be decreasing with emitter temperature. This could allow for efficient thermal-electric energy conversion devices, especially in the range of temperatures inaccessible to current energy conversion schemes.

To quantify the performance of a system like this we are interested in parameters such as efficiency and power density. Modeling the PV cell as an ideal thermodynamic diode operating at voltage V_o , and using Eq. (1), we can express the total radiative power exchange as [26]

$$P_{rad} = \frac{1}{\pi^2} \int_0^\infty dq q \left[\int_0^\infty d\omega \Pi(\omega, q) \frac{\hbar\omega}{e^{kT_1} - 1} - \int_{\omega_g}^\infty d\omega \Pi(\omega, q) \frac{\hbar\omega}{e^{\frac{\hbar\omega - eV_o}{kT_2}} - 1} \right] \quad (9)$$

In general, the optimal voltage V_o depends on other parameters in the system. We avoid the full optimization procedure, and, motivated by the observed dependence of efficiency on V_o , choose a voltage slightly below the limit $V_o^{max} = \omega_g(1 - T_2/T_1)$. The total electrical power generated in the photodiode is calculated as the product of the voltage V_o across the PV diode terminals, the electron charge e , and the difference between the absorbed photon flux and reradiated photon flux. This can be conveniently expressed as [26]

$$P_{PV} = \frac{1}{\pi^2} \int_0^\infty dq q \left[\int_{\omega_g}^\infty d\omega \Pi(\omega, q) \frac{eV_o}{e^{kT_1} - 1} - \int_{\omega_g}^\infty d\omega \Pi(\omega, q) \frac{eV_o}{e^{\frac{\hbar\omega - eV_o}{kT_2}} - 1} \right] \quad (10)$$

Finally, the efficiency of such a conversion scheme is defined as

$$\eta_{TPV} = \frac{P_{PV}}{P_{rad}} \quad (11)$$

We estimate the efficiency for several sets of parameters in Table 1. Plasma frequency, as well as the voltage across the PV diode, is approximately matched to the PV bandgap energy. Even though our analysis has been concerned with overcoming the black body limit and not necessarily maximizing the efficiency or the generated power density, the numbers for theoretical efficiency and power density compare well with more traditional energy conversion schemes. In thermoelectric systems one can achieve high power densities, but theoretical efficiencies are limited to 11% (16%) for $ZT = 1$ ($ZT = 2$) at $T = 600K$. In addition, there is a limit to operating temperature: $ZT = 2.5$ $\text{Bi}_2\text{Te}_3/\text{Sb}_2\text{Te}_3$ superlattice devices operate at hot-junction temperature of $300K$, while other high temperature TE alloys such as $\text{CeFe}_{3.5}\text{Co}_{0.5}\text{Sb}_{12}$ (temperature as high as $900K$) have ZT of up to 1.5 [27]. On the other hand, state of the art far field thermophotovoltaic devices can achieve theoretical efficiencies of 60% with ideal spectral control, but these systems do not have as high power density and require high emitter temperatures for optimal operation [28–30].

Table 1. Ideal plasmonic emitter-PV cell near-field TPV system: radiated power exchange, P_{rad} , generated electrical power P_{PV} , efficiency, and the flux ratio (relative to the transferred power between two black bodies in the far field), tabulated for a set of parameters, up to two significant digits. We assume $D = 10nm$, $\gamma = 0.01eV$.

$T_1 [K]$	$\omega_g [eV]$	$\omega_p [eV]$	$V_o [V]$	$P_{PV} [\frac{W}{cm^2}]$	$P_{rad} [\frac{W}{cm^2}]$	$\eta [\%]$	$\frac{H_{evan}}{H_{bb}}$
600	0.36	0.6	0.15	1.2	3.4	35	66
	0.17	0.35	0.08	14	39	36	150
1200	0.36	0.6	0.25	96	160	60	31
	0.17	0.35	0.12	250	470	53	55

With the ability to deliver both high efficiency and power density, as well as to operate in the intermediate ΔT range, near-field TPV systems could be a good complement to more conventional solid-state energy conversion schemes.

3. Alternative plasmonic thermal emitters

We have imposed no unusual requirement on the photovoltaic cell model so far. Semiconductors with gap frequencies and absorption coefficients we have mentioned so far can be readily found in nature. However, this is not true for the plasmonic emitter. For example, thermal excitation of surface plasmon modes is all but impossible in bulk metals, where plasma frequencies are in the ultraviolet range. In this section, we characterize the near-field transfer for silver as well as indium tin oxide (ITO) emitters, the latter being a promising plasmonic material in the near infra red.

We briefly note that by designing periodic structures, one could engineer an effective dielectric response which would mimic that of a surface plasmon at the desired frequency, so called *designer surface plasmons* or *spoof-surface-plasmons* (SSP) [31–33]. We postpone the detailed analysis of such systems to a future paper, and briefly mention that any SSP implementation would have to have very small feature size to accurately account for the behavior of highly evanescent modes responsible for the majority of near-field radiation transfer. We also note that TPV systems based on polar materials supporting surface phonon-polaritons, such as SiC, in conjunction with very low bandgap PV cells, have been analyzed before [17].

3.1. Silver

While the frequency of surface modes in silver is high, it is still possible for a TPV system with silver as emitter to reach transfer rates on the order of magnitude of those between two black bodies in the far field, especially for small separations. The mechanism behind this enhancement, however, is different. Unlike before, where extremely evanescent modes carried the bulk of radiation transfer, here it is not the excitation of surface plasmon-polaritons that is responsible for transfer in the near field. Figure 6(b) shows how this transfer depends on frequency ω and wave vector q . Here, we model permittivity of silver using a five-oscillator Lorentz-Drude (LD) model [34]. Given that surface plasmon frequency of silver is around 3.75eV [35], extremely high temperatures (on the order of several thousand kelvins) are required to excite these surface modes to the point where they would be the dominant mechanism in near-field energy transfer. This is impossible to achieve in practice, not least because the melting temperature of silver is approximately 1235K . Since surface plasmon modes are not excited, the

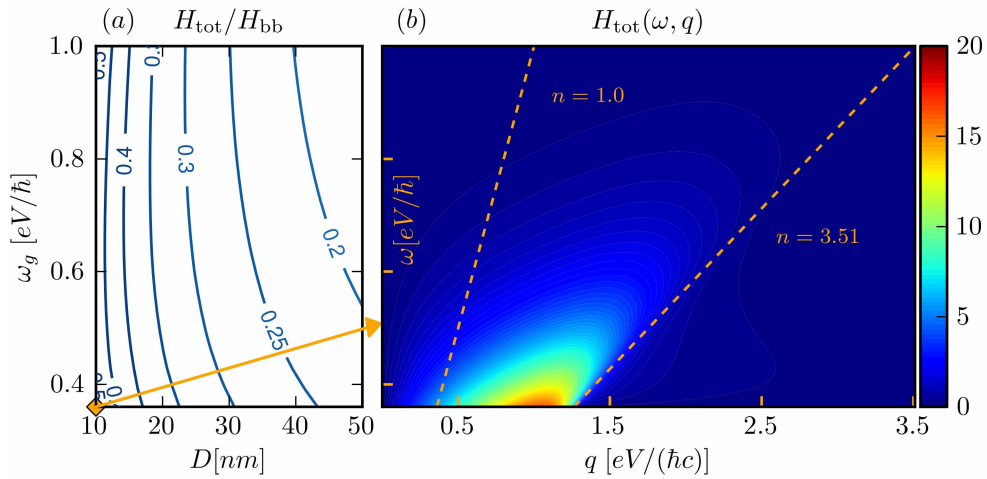


Fig. 6. Silver-PV near-field TPV system. (a) Radiation transfer ratio as a function of PV gap frequency ω_g and separation D , for $T_1 = 1235\text{K}$. (b) Contour plot of integrand in Eq. (1) and Eq. (2), as a function of ω , q in regions below and above the vacuum light line, respectively. This plot corresponds to H_{tot} for $\omega_g = 0.36\text{eV}$, $D = 10\text{nm}$ point from plot (a). The y-axis is shared between two plots. Two dashed lines correspond to light lines for $n = 1$ (vacuum) and $n = 3.51$ (PV cell).

majority of transfer occurs between two light lines corresponding to $n = 1$ and $n = 3.51$, with the latter being the static index of refraction of the PV cell. This is similar to the near-field transfer between two semi-infinite, low-loss, media of index of refraction n , where the maximum transfer is known to be n^2 times higher than the free space Planck distribution [16, 36]. Unlike before, high values of q are generally inaccessible, except for a small portion around the gap frequency, which is attributed to the non-zero value of optical absorption in the PV cell.

Figure 6(a) shows the transfer ratio dependence on gap frequency and separation. While the numerator H_{tot} now includes both the evanescent Eq. (1) and propagating Eq. (2) modes (i.e $H_{\text{tot}} = H_{\text{evan}} + H_{\text{prop}}$), the contribution of evanescent modes is still dominant, as observed in Fig. 6(b). Compared to the case of single, well-matched, plasmonic emitter, there is a much weaker dependence of the transfer ratio on gap frequency, indicating similar spectral transfer functions in H_{tot} and H_{bb} . This is, again, due to the lack of surface modes and highlights the difference in near-field energy transfer mechanisms.

3.2. Indium tin oxide (ITO)

Indium tin oxide is a promising plasmonic material in the near infrared (NIR) because its plasma frequency can be tailored by changing the doping level of tin [37–39]. Theoretical models, based on density functional theory, predict plasma frequencies in ITO as low as 0.44eV , for 45% (by weight) tin doping [38]. For this case, we model dielectric permittivity as $\epsilon(\omega) = \epsilon_\infty (1 - \omega_p^2/(\omega^2 + i\omega\gamma))$, with $\epsilon_\infty = 4$, $\omega_p = 0.44\text{eV}$, and estimated plasma damping of $\gamma \approx 0.1\text{eV}$ [37]. Qualitatively, the spectral near-field transfer with ITO as the emitter looks similar to that of Fig. 2(b). The main difference comes from the fact that the strong plasma damping coefficient in ITO broadens the spectral radiation transfer, as discussed in section 2.1.

For ITO emitter, and a PV cell with $\omega_g = 0.36\text{eV}$ (InAs), we obtain generated PV power, $P_{PV} = 0.36(34)\frac{W}{\text{cm}^2}$, efficiency $\eta = 12(45)\%$, and the transfer ratio $H_{\text{evan}}/H_{\text{bb}} = 20(11)$, for $T_1 = 600(1200)\text{K}$ and $V_o = 0.15(0.25)\text{V}$. We note that for $\epsilon_\infty = 4$, the ITO surface plasmon mode frequency is $\omega_p/\sqrt{1 + \epsilon_\infty^{-1}} \approx 0.39\text{eV}$. Broadened transfer spectrum, due to high plasma damping coefficient, results in higher thermalization losses in the PV cell, lowering efficiency compared to the pure plasmonic emitter in Table 1. Due to the broadband transfer, coupling the same ITO emitter to a lower bandgap PV cell would result in larger power density. However, the efficiency would be negatively affected, by the same argument as above.

Surface plasmon frequencies as low as 0.7eV have been experimentally measured in ITO [39]. We point out that dielectric properties of ITO are heavily dependent on sample preparation parameters and annealing conditions [37, 39]; however, the theoretical predictions for ITO presented above make it a potentially interesting material for near-field thermal emitters.

4. Exploiting surface plasmons in graphene

As mentioned, the main drawback to a described near-field TPV scheme is the lack of natural materials with plasmon frequencies in the desired near-IR range. Recently, it has been shown that graphene [40] can support surface plasmon modes, with tunable dispersion relation dependent on doping levels [41–43]. Furthermore, the near-field radiative energy transfer coefficient between graphene and amorphous SiO_2 has been argued to exceed that of the black body limit by ≈ 3 orders of magnitude [44, 45]. In Appendix B we argue that the same fluctuational electrodynamics expression in Eq. (1) can be used to analyze near-field radiation transfer between a suspended sheet of graphene and a PV cell. To model graphene, we assume its conductivity is independent of in-plane wave vector q , and consists of the drude (intraband) and interband conductivity, expressed respectively as [46]

$$\sigma_{\text{intra}}(\omega, T) = \frac{i}{\omega + i/\tau} \frac{e^2 2k_b T}{\pi \hbar^2} \ln \left[2 \cosh \frac{\mu}{2k_b T} \right] \quad (12)$$

$$\sigma_{\text{inter}}(\omega, T) = \frac{e^2}{4\hbar} \left[G \left(\frac{\hbar\omega}{2} \right) + i \frac{4\hbar\omega}{\pi} \int_0^\infty \frac{G(\epsilon) - G(\hbar\omega/2)}{(\hbar\omega)^2 - 4\epsilon^2} d\epsilon \right] \quad (13)$$

where $G(\epsilon) = \sinh(\epsilon/k_b T)/(\cosh(\mu/k_b T) + \cosh(\epsilon/k_b T))$. Here, μ is the chemical potential and τ the relaxation time which takes into account various electron scattering processes. The fact that graphene is a poor absorber in the far field (and hence a poor emitter) allows us to, as before, restrict our analysis to p -polarized evanescent modes.

In Fig. 7 we demonstrate the near-field radiation transfer between a sheet of graphene at T_1 and the PV cell held at room temperature. We model the PV cell in the same manner, Eq. (3), with $\omega_g = 0.17\text{eV}$ and $\alpha_0 = 0.7 \times 10^4 \text{cm}^{-1}$ (InSb). Using a low bandgap PV cell allows us to better demonstrate the effects of graphene doping on near-field radiation transfer. In Fig. 7(a) we plot the integrand in the spectral transfer function $H(\omega, q)$ to reveal the modes that dominate the near-field transfer. We observe that the main contribution consists of a set of modes situated

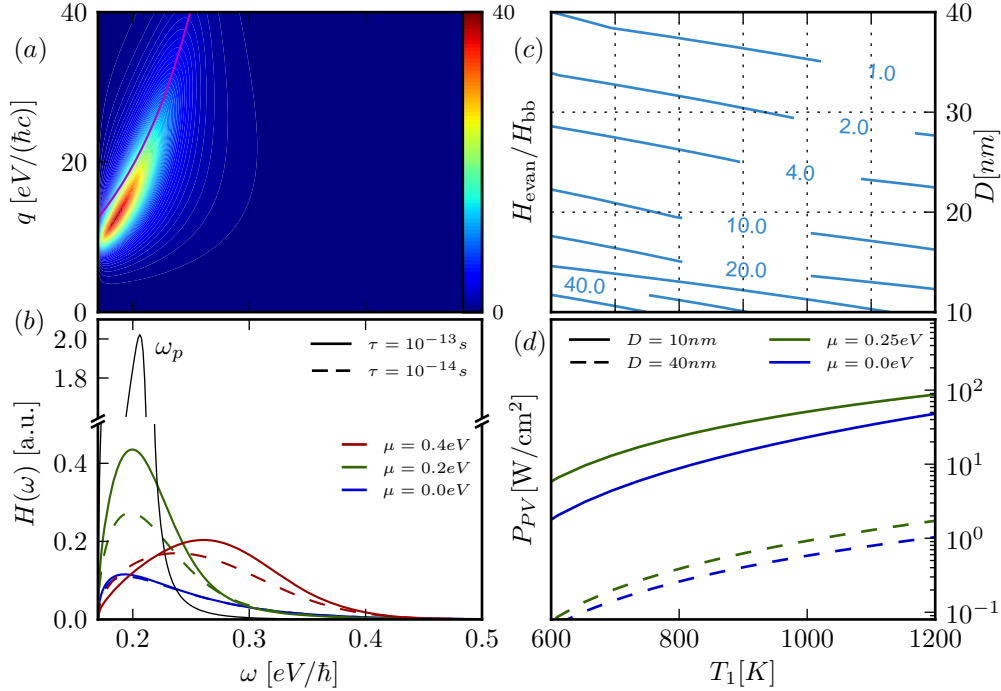


Fig. 7. Graphene-PV near-field TPV system. (a) Contour plot of integrand $H(\omega, q)$ in Eq. (1) as a function of ω, q for parameters $T_1 = 600K, D = 10nm, \mu = 0.2eV$ and $\tau = 10^{-13}s$. PV cell parameters are $\omega_g = 0.17eV, \alpha_0 = 0.7 \times 10^4 cm^{-1}$. Solid (magenta) line is the vacuum surface plasmon dispersion relation, Eq. (14), for the graphene sheet. (b) $H(\omega)$ evaluated for different parameters with T_1, D same as in (a). For comparison, black ω_p -line demonstrates $H(\omega)$ for a pure plasmonic emitter analyzed in section 2, with $\omega_p = 0.3eV$. (c) Contour plot of the heat transfer ratio vs. the two black bodies in the far field, as a function of T_1 and D . In (c) and (d), $\tau = 10^{-13}s$ and doping is $\mu = 0.25eV$. (d) Electric power generated P_{PV} as a function of T_1 where the voltage across the PV diode terminals is $V_o = 0.08V$. The x -axis is shared between plots (a), (b) and plots (c), (d), respectively.

around the dispersion relation for plasmons in an isolated, suspended, sheet of graphene [41]

$$q = \epsilon_0 \frac{2i\omega}{\sigma(\omega, T)} \quad (14)$$

This strong localization of surface plasmons in isolated graphene is in contrast to what we observed in the dispersion relation for an isolated pure plasmonic material (section 2) in Fig. 2, where characteristic parallel wave vectors were much smaller, i.e. the surface plasmon in air was a lot less evanescent. To highlight the relationship between spectral control and graphene doping, in Fig. 7(b) we show the spectral cross-section for a given frequency $H(\omega)$, similar to Eq. (7), only integrated over wave vectors q . The total transfer may then be written as $H_{\text{evan}} = \int_{\omega_g}^{\infty} H(\omega) d\omega$, i.e. $H(\omega)$ includes the Boltzmann factor $\Theta(\omega, T)$. We observe that doping plays an important role in shifting the spectral transfer to desired frequencies, much like the plasma frequency in the case of a pure plasmonic emitter. For a PV cell with bandgap of $0.17eV$, an intermediate doping level of $\mu = 0.2eV$ appears to be better suited for near-field radiation transfer than either the case of higher doping ($\mu = 0.4eV$) or no doping. While highly evanescent modes dominate the transfer for both graphene and pure plasmonic emitter, spec-

tral transfer is broader in the former case. The narrow peak, corresponding to $\omega_p = 0.3eV$, shows that a pure plasmonic material is still better suited for frequency selectivity than doped graphene. We also note that increased scattering (lower relaxation time τ ; by an order of magnitude in this case) broadens the spectral cross-section, but not by an order of magnitude.

In Fig. 7(c), we look at the integrated transfer and, as before, compare it to the far field transfer between two black bodies. Similarly to the case for optimized plasmon frequency in Fig. 5, we observe that transfer mediated by plasmons in graphene grows slower with emitter temperature than that of two black bodies in the far field. More important than the emitter temperature is the separation D . Significant, order-of-magnitude increases are obtained as two surfaces are brought closer together, not just for flux ratio, but for power density as well, as shown in Fig. 7(d). Appropriately tuning the doping energy to the PV cell bandgap frequency is important, but bringing the graphene surface close to the emitter is particularly beneficial.

We show the results for efficiency and power density for graphene-as-emitter TPV system in Table 2 (a more detailed optimization over the chemical potential and the relaxation time is carried out in Appendix C). For comparison, we also show the results for the case when the

Table 2. Comparison between a silicon-PV and a graphene-PV near field TPV system: radiated power exchange, P_{rad} , generated electrical power P_{PV} , efficiency, and the flux ratio (relative to the transferred power between two black bodies in the far field), tabulated for a set of parameters, up to two significant digits. We assume $D = 10nm$, $\tau = 10^{-13}s$.

$T_1 [K]$	$\omega_g [eV]$	$\mu [eV]$	$V_o [V]$	Si - PV				graphene - PV			
				$P_{PV} [\frac{W}{cm^2}]$	$P_{rad} [\frac{W}{cm^2}]$	$\eta [\%]$	$\frac{H_{evan}}{H_{bb}}$	$P_{PV} [\frac{W}{cm^2}]$	$P_{rad} [\frac{W}{cm^2}]$	$\eta [\%]$	$\frac{H_{evan}}{H_{bb}}$
600	0.36	0.4	0.15	0.20	8.5	2.3	12	0.22	0.7	32	13
	0.17	$\frac{0.25}{0}$	$\frac{0.08}{0.08}$	1.3	9.4	14	14	6.0	17	35	62
1200	0.36	0.4	0.25	30	130	23	11	22	38	57	7.3
	0.17	$\frac{0.4}{0}$	$\frac{0.12}{0.12}$	43	150	29	13	120	300	40	31
								61	140	43	15

emitter is pure silicon, with $n_{Si} = 4$. In the case of silicon, the ω - q profile of the near-field transfer is very similar to that of Fig. 6(b) (i.e. broadband in frequency), with parallel wave vectors limited by $n_{Si} = 4$ light line. As a result, both the evanescent and propagating, as well as s and p polarized, modes contribute to power transfer when the emitter is silicon (or silver). For graphene, only p polarized, evanescent modes are relevant.

From Table 2, we observe that lowering the bandgap increases the overall power transfer, as in the case of a pure plasmonic emitter (Table 1). For both the plasmonic emitter and graphene, we attribute high efficiencies to the fact that very evanescent modes, that dominate the near-field transfer, carry negligible power for frequencies below the band gap, where the PV cell does not absorb and the parallel wave vectors are limited by the n_{PV} light line. For graphene, both efficiency and power density are lower than in Table 1, confirming that a graphene emitter does not have as good spectral control. However, the results are promising, especially considering there are, save for experimental difficulties, no fundamental physical limitations to implementing a graphene-based near field TPV system.

5. Conclusion

In this manuscript, we analyzed several different implementations of a high-efficiency near-field TPV system. In the case of a pure plasmonic emitter we found that the best improvement, over the transfer between two black bodies in the far field, is achieved for low bandgap PV cells,

and emitter plasmon frequencies optimally matched to the bandgap. Ability to control plasmon damping is also beneficial as, contrary to other applications, higher values of plasmon damping can significantly increase the near-field power transfer. While we focused on bulk semiconductor PV cells, we discussed the requirements for an ideal near-field PV cell. Realizing that materials with the plasma frequency in the frequency range of interest cannot be found in naturally occurring bulk materials, we reiterated that metals, such as silver, would not be a suitable replacement due to difficulties of thermally exciting relevant surface modes. Besides indium tin oxide, a promising alternative to a pure plasmonic emitter is graphene, where, by doping, the dispersion relation can be tuned to match the PV cell bandgap. Separation gap remains an important parameter in all cases, as significant, order-of-magnitude enhancement over the black body transfer is achieved only for separations on the order of tens of nanometers. High theoretical efficiencies ($\approx 40\%$) compared to conventional thermoelectrics, as well as high power densities ($120 \frac{W}{cm^2}$ at $T = 1200K$ hot-side) compared to state-of-art far field TPV systems, in addition with the ability to operate in the intermediate ($600 - 1200K$) emitter temperature range, make this a promising power conversion technology. We also note a potential application of near-field radiation transfer in increasing the efficiency of thermoelectric devices by selectively heating only the electrons and not the phonons [47].

The authors would like to acknowledge helpful discussions with Hrvoje Buljan, Peter Bermel, Bo Zhen, Gang Chen, Alejandro Rodriguez and Steven Johnson. OI and MS were partially supported by the MIT S3TEC Energy Research Frontier Center of the Department of Energy under Grant No. DE-SC0001299. MJ was supported in part by the Croatian Ministry of Science under Grant No. 119-0000000-1015. This work was also partially supported by the Army Research Office through the Institute for Soldier Nanotechnologies under Contract No. W911NF-07-D0004, and the Unity through Knowledge Fund Grant Agreement No. 93/11.

Appendix A

In this appendix we review the derivation of the expression for the spectral transfer function, Eq. (5). The main approximation in deriving this result is that $q \gg \omega/c$, i.e. we focus on modes in the extreme near field. This allows us to approximate the p -mode reflection coefficient at the i -0 interface ($i = 1, 2$ for emitter, PV cell, respectively; Fig. 1) as $r_{0i}^p \approx \frac{\epsilon_i - 1}{\epsilon_i + 1}$. With this in mind, spectral transfer function from Eq. (1) becomes,

$$\Pi(\omega, q) = \frac{\text{Im}\left(\frac{\epsilon_1 - 1}{\epsilon_1 + 1}\right) \text{Im}\left(\frac{\epsilon_2 - 1}{\epsilon_2 + 1}\right)}{\left|1 - \left(\frac{\epsilon_1 - 1}{\epsilon_1 + 1}\right) \left(\frac{\epsilon_2 - 1}{\epsilon_2 + 1}\right) e^{-2qD}\right|^2} e^{-2qD} \quad (15)$$

For the PV interface, we define $(\epsilon_2 - 1)/(\epsilon_2 + 1) \equiv \chi' + i\chi''$. To derive the dispersion relation for this system, we rely on the fact that $\chi' \approx \text{const}$ in the range of frequencies of interest, and also $\chi''(\omega) \ll \chi'$. In addition, we simplify the expression for the reflection coefficient at the plasmonic emitter interface in two limits of plasmon damping γ ,

$$\frac{\epsilon_1(\omega) - 1}{\epsilon_1(\omega) + 1} = \begin{cases} \frac{\omega_p^2}{\omega_p^2 - 2\omega^2} \left[1 + \frac{2i\omega\gamma}{\omega_p^2 - 2\omega^2}\right] & \text{if } \gamma \ll \frac{\omega_p^2 - 2\omega^2}{2\omega} \\ \frac{i\omega_p^2}{2\omega\gamma} \left[1 - \frac{i(\omega_p^2 - 2\omega^2)}{2\omega\gamma}\right] & \text{if } \gamma \gg \frac{\omega_p^2 - 2\omega^2}{2\omega} \end{cases} \quad (16)$$

The dispersion relation for this system, obtained from the the pole of Eq. (15), can be approximated as

$$\omega_0(q) = \frac{\omega_p}{\sqrt{2}} \sqrt{1 - \chi' e^{-2qD}} \quad (17)$$

Using Eqns. (15-17), we obtain the approximation for $\Pi(\omega)$, given by Eq. (5). Defining $\beta_0 = \frac{\omega_p^2 - 2\omega_0^2}{2\omega_0}$, such that $\beta = \beta_0 \frac{\chi''}{\chi'}$, we observe that for low frequencies, β_0 imposes the condition on γ , that is $\gamma \ll \beta_0$ for the approximation in Eq. (16) to hold. Its maximum value is $\beta_0^{MAX} = \frac{\omega_p^2 - 2\omega_g^2}{2\omega_g}$ (increases with decreasing frequency) where ω_g is the PV gap frequency, and gives the upper bound on γ in the low frequency range. In the high frequency limit, $\omega \approx \omega_p/\sqrt{2}$, such condition on γ does not exist, and, generally, Eq. (5) remains valid for even higher values of γ (up to $\approx 0.1eV$). In both γ limits in Eq. (16), $\Pi(\omega, q)$ is correctly approximated by Eq. (5), as well as in the intermediate range of γ , making it, in general, a good approximation of Eq. (1). Finally, Eq. (5) is a quasi-lorentzian, because β , in general, is a function of frequency. However, due to small variation of χ'' (Fig. 4) on the scale of $\gamma + \beta$, it is often safe to write $\beta(\omega) \approx \beta(\omega_0)$.

We briefly note that when both media are plasmonic (i.e. $\epsilon_2 = \epsilon_1$), the dispersion relation for this problem can be obtained in a similar way [21], and for $\omega < \omega_p/\sqrt{2}$ is given by,

$$\omega_0(q) = \frac{\omega_p}{\sqrt{2}} \sqrt{1 - e^{-qD}} \quad (18)$$

With this in mind, the spectral transfer function becomes

$$\Pi(\omega, q) = \frac{(\gamma/2)^2}{4(\omega - \omega_0(q))^2 + \gamma^2} \quad (19)$$

It is now easy to understand the effect of γ : while the peak of lorentzian in Eq. (19) is constant, damping broadens the spectral transfer function Π , increasing the overall integral in Eq. (1). Assuming γ is small enough, such that $\Theta(\omega_0 \pm 2\gamma, T) \approx \Theta(\omega_0, T)$, we can integrate Eq. (19) to get

$$\int d\omega \Pi(\omega, q) = \frac{\gamma}{4} \left[\pi + 2 \tan^{-1} \left(\frac{2\omega_0}{\gamma} \right) \right] \quad (20)$$

which, for $\gamma \ll \omega_0$, equals $\gamma\pi/2$, and scales linearly with γ .

Appendix B

In this section, we briefly show how, using the same fluctuational electrodynamics approach, the expression for the near-field radiation transfer between a suspended graphene sheet and an arbitrary semi-infinite medium reduces to Eq. (1). We recall how the spectral transfer is calculated: (i) we first derive the Green's function relating the electric and the magnetic field to the thermally induced currents in graphene, (ii) we estimate, using the fluctuation-dissipation theorem, the correlation between these random currents, and finally, (iii) we calculate the Poynting vector to obtain the net flux between two structures. Following the formalism of Sipe [48], the electric and the magnetic field in each medium is split into an upward and a downward propagating wave. The unit vectors for the electric field of the s and p polarized wave are $\hat{s} = \hat{q} \times \hat{z}$ and $\hat{p}_{i\pm} = (q\hat{z} \mp k_{zi}\hat{q})/k_i$ in medium i , respectively. An electric current sources in medium 1 would generate fields in medium 2, a distance D away, according to the relation [49]

$$\mathbf{E}(r, \omega) = \int d^3 r' \mathbf{G}^E(r, r', \omega) \mathbf{j}(r') \quad (21)$$

$$\mathbf{H}(r, \omega) = \int d^3 r' \mathbf{G}^H(r, r', \omega) \mathbf{j}(r') \quad (22)$$

where [49]

$$\mathbf{G}^E(r, r', \omega) = \frac{-\omega\mu_0}{8\pi^2} \int d^2q \frac{1}{k_{z1}} (\hat{s}T_s\hat{s} + \hat{p}_{2+}T_p\hat{p}_{1+}) e^{iq(r_q-r'_q)+ik_{z2}(z-D)-ik_{z1}z'} \quad (23)$$

$$\mathbf{G}^H(r, r', \omega) = \frac{-n_2\omega}{8\pi^2c} \int d^2q \frac{1}{k_{z1}} (-\hat{p}_{2+}T_s\hat{s} + \hat{s}T_p\hat{p}_{1+}) e^{iq(r_q-r'_q)+ik_{z2}(z-D)-ik_{z1}z'} \quad (24)$$

Here n_i is the index of refraction of medium i , and $T_{s,p}$ is the generalized Fresnel transmission coefficient for a two interface system, given by [48]

$$T = \frac{t_{10}t_{02}e^{ik_{z0}D}}{1 - r_{02}r_{01}e^{2ik_{z0}D}} \quad (25)$$

where t_{ij}, r_{ij} are transmission and reflection coefficients, respectively, on the i - j interface. This expression is valid for both s and p polarization. To obtain the expression for the radiation transfer to medium 2, we calculate the Poynting vector flux just above 0-2 interface, at $z = D^+$. The Poynting vector involves products of the form $E_\alpha H_\beta^*$ which in turn contain current density product terms $j_\alpha j_\beta$. The spatial correlation function between different current density sources, in medium of conductivity σ and at temperature T , is given by the fluctuation dissipation theorem [50]

$$\langle j_\alpha^*(r, \omega) j_\beta(r', \omega') \rangle = \frac{\Theta(\omega, T)}{2\pi} [\sigma(\omega) + \sigma^*(\omega)] \delta(r - r') \delta(\omega - \omega') \delta_{\alpha\beta} \quad (26)$$

With this in mind, using Eqns. (21)-(24) and writing graphene conductivity as $\sigma\delta(z)$, we can express the z -component of the Poynting vector as [49]

$$S_z = 2\text{Re} (E_x H_y^* - E_y H_x^*) \quad (27)$$

where

$$E_x H_y^* - E_y H_x^* = \frac{n_2^* \omega^2 \mu_0}{c(8\pi^2)^2} \int d^3r' \int d^2q d^2q' \frac{1}{|k_{z1}|^2} [g_{x\alpha}^E g_{y\alpha}^{H*} - g_{y\alpha}^E g_{x\alpha}^{H*}] \\ \times \frac{\Theta(\omega, T_1)}{2\pi} [\sigma + \sigma^*] \delta(z') e^{i(q-q')(r_q-r'_q)} e^{ik_{z1}(z-D)} e^{-ik_{z1}z'} e^{-ik_{z2}^*(z-D)}$$

where $\alpha = x, y$ (no induced current in the z direction in graphene) and we introduced the shorthand notation for the dyadics

$$\mathbf{g}^E = \hat{s}T_s\hat{s} + \hat{p}_{2+}T_p\hat{p}_{1+} \quad (28)$$

$$\mathbf{g}^H = -\hat{p}_{2+}T_s\hat{s} + \hat{s}T_p\hat{p}_{1+} \quad (29)$$

For suspended graphene ($n_1 = n_0 = 1$), we calculate the expression above and obtain

$$g_{x\alpha}^E g_{y\alpha}^{H*} - g_{y\alpha}^E g_{x\alpha}^{H*} = |T_s|^2 \frac{k_{z2}^*}{n_2^* k_0} + |T_p|^2 \frac{k_{z2}}{n_2 k_0} \frac{|k_{z1}|^2}{k_0^2} \quad (30)$$

Integrating over r' and q' , evaluating at $z = D^+$ and taking the real part of Eq. (28), together with following relations for suspended graphene [46]

$$r_p^G = \frac{1 - \varepsilon_G}{\varepsilon_G}, \quad t_p^G = \frac{1}{\varepsilon_G}, \quad \text{where } \varepsilon_G = 1 + \frac{\sigma k_{z0}}{2\varepsilon_0\omega} \quad (31)$$

and

$$2\omega \frac{\text{Im}(r_p^G)}{\text{Im}(k_{z0})} = |t_p^G|^2 \frac{\text{Re}(\sigma)}{\epsilon_0} \quad (32)$$

we recover Eq. (1). Above derivation focuses on p -polarized, evanescent ($q > \omega/c$) modes, which contribute the most to the radiation transfer in the near field. An alternative way to derive the near-field transfer in the case of graphene is to calculate, using reciprocity, the radiative power exchange when medium 2 is the emitter. We then estimate the absorbed power in the graphene sheet as the product of its conductivity σ and the surface current density that in-plane, q -component of the electric field at $z = 0$ would induce. This approach confirms Eq. (1).

Appendix C

Optimizing the heat transfer ratio as a function of chemical potential μ and relaxation time τ (Fig. 8) leads to several conclusions. First, flux ratios calculated using $\mu = 0.25eV$ and $\tau = 10^{-13}s$ (Fig. 7 and Table 2) for $T_1 = 600(1200)K$ were close to their respective optimal values. Second, slow variation of the optimal flux ratio as a function of chemical potential is consistent with the broadband nature of spectral transfer in the case of graphene versus the pure plasmonic emitter (Fig. 7(b)). Finally, leveling of the flux ratio for high enough values of relaxation time, with a reduction in impurity or phonon scattering, indicates a transition to loss processes dominated by interband transitions (13).

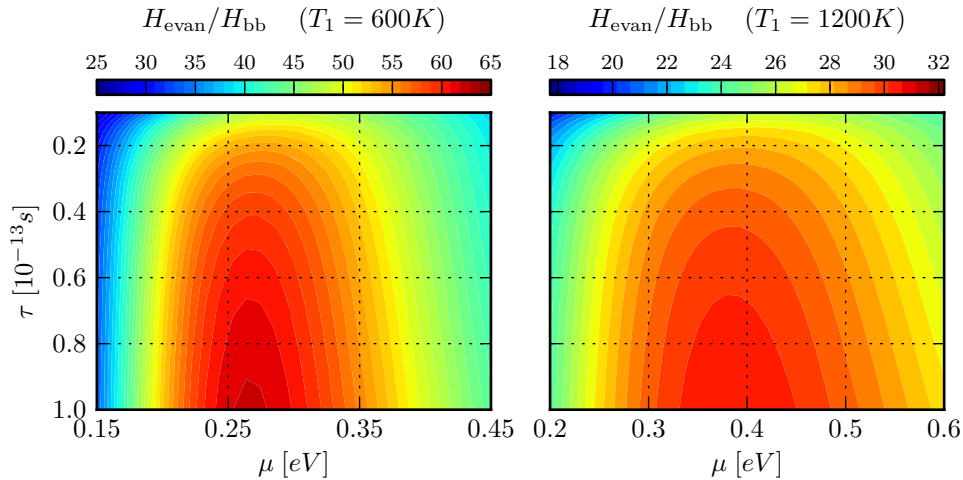


Fig. 8. Optimization of the flux ratio $H_{\text{evan}}/H_{\text{bb}}$ for graphene-PV near-field TPV system, where $\omega_g = 0.17eV$, $D = 10nm$.